LANGMUIR

pubs.acs.org/Langmuir
Article

Binding of Urinary Human Serum Albumin Fragments to Albumin-Selective Aptamer-Bound Graphene Quantum Dots: Simulation Studies

Chanya Archapraditkul, Deanpen Japrung,* and Prapasiri Pongprayoon*

Cite This: *Langmuir* 2025, 41, 11081−11089
Read Online

ABSTRACT: Microalbuminuria is a key indicator of chronic kidney disease (CKD), resulting from the leakage of albumin into urine. The accuracy of microalbuminuria measurement depends on urine freshness as improper storage and slow processing can lead to protease digestion of albumin. Recently, graphene-based aptasensors have been shown to detect albumin in aged urine samples, suggesting that albumin fragments can still be recognized by these sensors. To date, nine urinary albumin fragments (F1−F9) have been reported. Meanwhile, the graphene quantum dot (GQD) has emerged as a promising material due to its noncytotoxicity, high biocompatibility, and intrinsic fluorescence properties. Its comparable size to aptamers makes it particularly attractive for albumin detection. In this study, molecular dynamics (MD) simulations were performed to reveal the binding modes of urinary albumin fragments (F1−F9) to the aptamer-bound GQD (GQDA) complex. The study compares the binding behavior of nonaggregated (N_AG) and preaggregated (AG) albumin fragments with GQDA. The results demonstrate that the spontaneous clustering of GQDA and albumin fragments occurs in all cases. However, aggregated fragments exhibit reduced aptamer accessibility due to geometric confinement and structural rigidity. Lysine-rich regions were found to play a crucial role in fragment−aptamer interactions, with F1 and F8 displaying the highest number of aptamer contacts. Notably, F8, the most stable fragment, showed the strongest interactions with aptamers, highlighting its potential as a urinary biomarker for CKD detection. The findings from this study provide valuable molecular insights into the interactions between urinary albumin fragments and GQDA, paving the way for the development of highly selective and sensitive CKD diagnostic platforms.

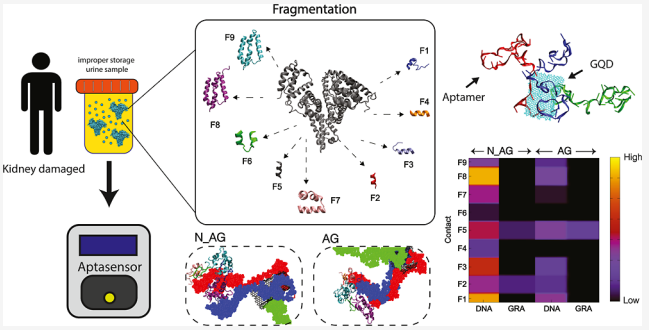

INTRODUCTION

Microalbuminuria is a major indicator of chronic kidney disease (CKD).[1] This condition is caused by albumin leaks into urine. The increase in the microalbuminuria level in urine is associated with progressive renal function loss.[2] Current guidelines for CKD recommend using the microalbuminuria level and glomerular filtration rate (eGFR) to identify the CKD stage. It has been reported that the early detection of microalbuminuria in patients is cost-effective.[3,4] The urine dipsticks can offer a rapid point-of-care (POC) screening test kit when there are limited resources and laboratory analyses. Urine dipsticks are semiquantitative methods that measure the albuminuria or express data as the albumin-to-creatinine ratio (ACR), providing only quantitative analysis.[5−9] Most quantitative and qualitative microalbuminuria assays are based on immunoassays, which require antibodies to bind albumin in urine. The accuracy of these assays depends on urine freshness since the albumin samples improperly stored and processed slowly can undergo protease digestion, leading to inaccurate ACR results.[10−12] Therefore, there is a growing need for innovative diagnostic platforms that can detect albumin fragments in aged urine samples.

Human serum albumin (HSA), the most abundant protein in human plasma, consists of 585 amino acids. HSA is divided into three homologous domains (I, II, and III). Each domain is subdivided into two subdomains (A and B; Figure 1A). In urine, nine albumin fragments (F1−F9) were experimentally identified[13] (Figure 1A). F1−F7 are short fragments, while F8 and F9 belonging to subdomain IIIB are large. Some of these fragments were found to be potential biomarkers for cancer and diabetes.[13−15] Previous computational studies illustrated that the largest fragment (F8) is the most stable across a wide range of urinary pH conditions (4.5−8.0).[16] More recently, our study illustrated that a graphene-based fluorescent

Received: February 12, 2025
Revised: April 14, 2025
Accepted: April 15, 2025
Published: April 23, 2025

https://doi.org/10.1021/acs.langmuir.5c00732
Langmuir 2025, 41, 11081−11089

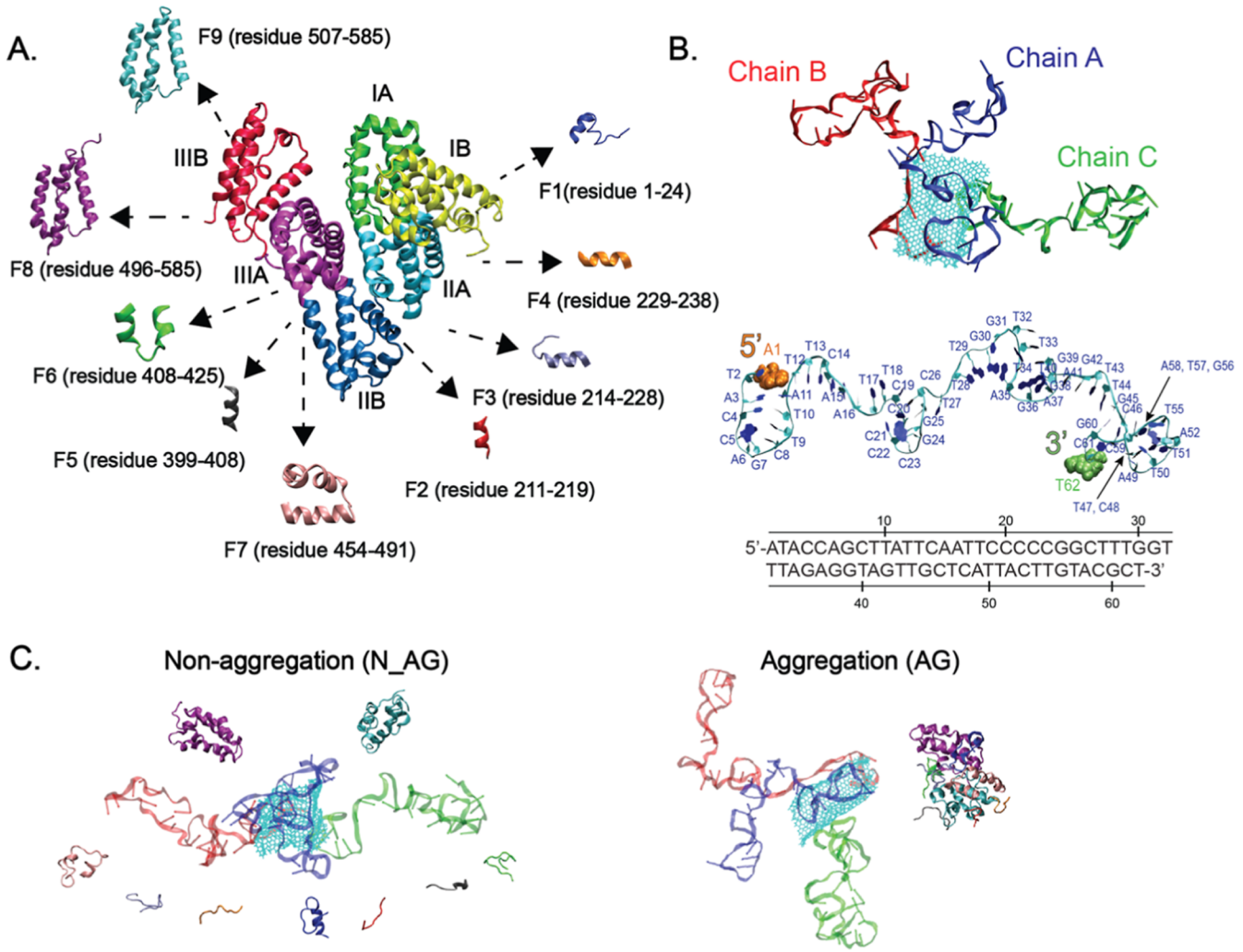

Figure 1. (A) Cartoon views of HSA and all fragment (F1−F9) structures. (B) Three albumin-selective DNA aptamers in complex with GQD. Each aptamer with sequences is also displayed. (C) Two initial locations of HSA fragments (nonaggregation (N_AG) (left) and aggregation (AG) (right) systems) around an aptamer−GQD complex (GQDA).

aptasensor, employing an aptamer specifically designed to bind albumin (aptamer sequences are shown in Figure 1B), can detect albuminuria even in stored urine samples.[11] This suggests that aptamers may bind to certain albumin fragments, enabling albuminuria detection in nonfresh urine. This versatility is particularly beneficial for remote sample collection, where immediate processing is not feasible.

Graphene-based fluorescent aptasensors are among the most promising strategies to detect protein analytes including albumin due to their sensitivity, selectivity, and cost-effectiveness.[11,17−20] In the graphene-based fluorescent aptasensor, fluorescent dye-attaching aptamers (the recognition element) adhere to the graphene surface and become quenched. Albumin in a sample then binds to aptamers and triggers the albumin−aptamer desorption, resulting in the recovery of fluorescent intensity, which can be correlated with the albuminuria level. A number of graphene-based aptasensors for albumin detection have been reported.[19,21−24] Recently, nanosized graphene or graphene quantum dots (GQDs) have been discovered.[25,26] These nanosized GQDs have been rapidly of interest due to their noncytotoxicity, unique photoluminescence properties, and high biocompatibility.[27−30] These promising properties allow the involvement of GQDs in several disease biosensor platforms, including albumin detection.[17,31−35] In addition, previous studies reported that the use of GQD generates the geometric confinement of short RNAs on a GQD surface, which can promote easy desorption and probe accessibility.[36,37]

In a previous study,[11] we demonstrated that our developed graphene-based aptasensor could detect albumin in urine samples stored for up to 3 days at room temperature (25 °C), up to 7 days at 4 °C, and over 12 months at −80 °C. This finding suggests that albumin degradation does not fully eliminate the aptamer binding site, allowing for reliable detection even in nonfresh urine. Additionally, we analyzed the protease digestion of albumin using Asp-N endopeptidase, a common protease found in urine. Our results showed that the long-digested fragments primarily originated from domain IIIB, which is comparable to the F8 fragment identified in a previous study.[13] Moreover, our previous computational study demonstrated that F8 is the most stable fragment among all nine albumin fragments (sequences are listed in Table 1) across various pH ranges. These findings support the hypothesis that the aptamer can still recognize albumin fragments after protease digestion, providing a strong

https://doi.org/10.1021/acs.langmuir.5c00732
Langmuir 2025, 41, 11081−11089

Table 1. Sequences of All Fragments (F1−F9)[a]

Fragment	Residue no.	Sequence	Net charges at pH 7
F1	1-24	DAHKSEVAHRFKDLGEENFKALVL	-1
F2	211-219	FKAWAVARL	+1
F3	214-228	WAVARLSQRFPKAEF	+2
F4	229-238	AEVSKLVTDL	-1
F5	399-408	GEYKFQNALL	0
F6	408-425	LVRYTKKVPQVSTPTLVE	+2
F7	454-491	SVVLNQLCVLHEKTPVSDRVTKCCTESLVNRRP CFSAL	+2
F8	496-585	TYVPKEFNAETFTFHADICTLSEKERQIKKQTAL VELVKH KPKATKEQLKAVMDDFAAFVEKCCKADDKETC FAEEGKKLVAASQAALGL	0
F9	507-585	FTFHADICTLSEKERQIKKQTALVELVKHKPKAT KEQLKAVMDDFAAFVEKCCKADDKETCFAEEG KKLVAASQAALGL	+1

[a]The net charge at each pH is also shown. Cysteines in some sequences are underlined. Negatively and positively charged residues are labelled in red and blue, respectively.

foundation for developing an aptasensor capable of detecting albumin degradation products in urine.

In that study, graphene sheets were used as the aptamer substrate, providing a strong fluorescence quenching effect and enabling albumin detection. However, graphene sheets have limitations, particularly in size compatibility with biomolecules and surface interaction efficiency with fragmented albumins. Building on this foundation, the present study explores GQD as an alternative aptamer substrate. GQD offers several advantages over graphene sheets, including smaller size, better water dispersibility, and intrinsic photoluminescence properties. Their comparable size to aptamers and albumin fragments may facilitate stronger interactions and enhance aptasensor performance. Additionally, our previous study has shown that aptamer saturation on the GQD surface is crucial for aptasensor performance.[38] Therefore, we employ an aptamer-saturated GQD in this work.

Our previous study also found that all fragments can cluster in a solution. Therefore, it is essential to investigate whether aggregated (AG) and nonaggregated (N_AG) albumin fragments can still be recognized by the aptamer−GQD complex (the simulation setup is shown in Figure 1C). Protein aggregation is commonly observed in biological systems,[39−44] and understanding its impact on aptamer binding is essential for developing robust biosensors.

To gain molecular-level insights into these interactions, molecular dynamics (MD) simulations were performed, allowing us to model the binding behavior of albumin fragments to the aptamer−GQD complex under different conditions. The insights from this study will contribute to the development of GQD-based fluorescent aptasensors with enhanced sensitivity and specificity for CKD screening and monitoring.

MATERIALS AND METHODS

Aptamer-Saturated GQD Complex (GQDA) Preparation. The 62-nucleotide ssDNA albumin-selective aptamer (5′-ATA CCA GCT TAT TCA ATT CCC CCG GCT TTG GTT TAG AGG TAG TTG CTC ATT ACT TGT ACG CT −3′) was obtained from previous studies.[11,23,24] The three-dimensional structure of the aptamer was built using the 3D-DART server[45] and equilibrated in solution for 10 ns to obtain a stable aptamer structure (see Figure S1A for the RMSD of an aptamer).

A GQD was placed at the center of a cubic box with dimensions of 20.4 × 20.4 × 20.4 nm^3, and then six aptamers were placed at least 1 nm away from each other and from the GQD (Figure S1B in the Supporting Information). The topology of the GQD was obtained from a previous work.[38] GQD and aptamers were soaked in TIP3P water molecules and counterions and neutralized by 1 M NaCl. The system was equilibrated for 10 ns, followed by a 500 ns production run (the simulation setting can be seen in the Simulation Protocols section). Only three aptamers (chains A−C) adhered to the GQD, while the rest were in the bulk. The three aptamers adhered to GQD throughout the 500 ns simulations (Figure S1B in the Supporting Information). This indicates the aptamer-saturated GQD. The final snapshot of the GQD−aptamer (GQDA) complex was used for further simulations.

Preparation of Fragmented Albumins (F1−F9)−GQDA Systems. The three-dimensional structures of the nine fragments (F1−F9) were obtained from a previous work,[13] where the final snapshots of all fragments at 1000 ns were used here. The sequences and charges of each fragment are listed in Table 1. These fragments were generated from a crystal structure downloaded from the Protein Data Bank (PDB code: 1E78). In a previous work,[16] spontaneous fragment aggregation was found under all pH conditions. Thus, in this work, the binding mechanisms of nonaggregated (N_AG) and aggregated (AG) albumin fragments with GQD are studied for comparison. Only binding at physiological pH (pH 7.0) is studied here. For the nonaggregation system (N_AG), each fragment was placed at least 1 nm away from the GQDA complex, whereas the aggregated fragments (AG) were placed 1 nm from GQDA (measured from the nearest surface of a fragment cluster to the GQDA surface). Each system was placed into a 19.9 × 19.9 × 19.9 nm^3 cubic box and subsequently soaked in TIP3P water molecules,

https://doi.org/10.1021/acs.langmuir.5c00732
Langmuir 2025, 41, 11081−11089

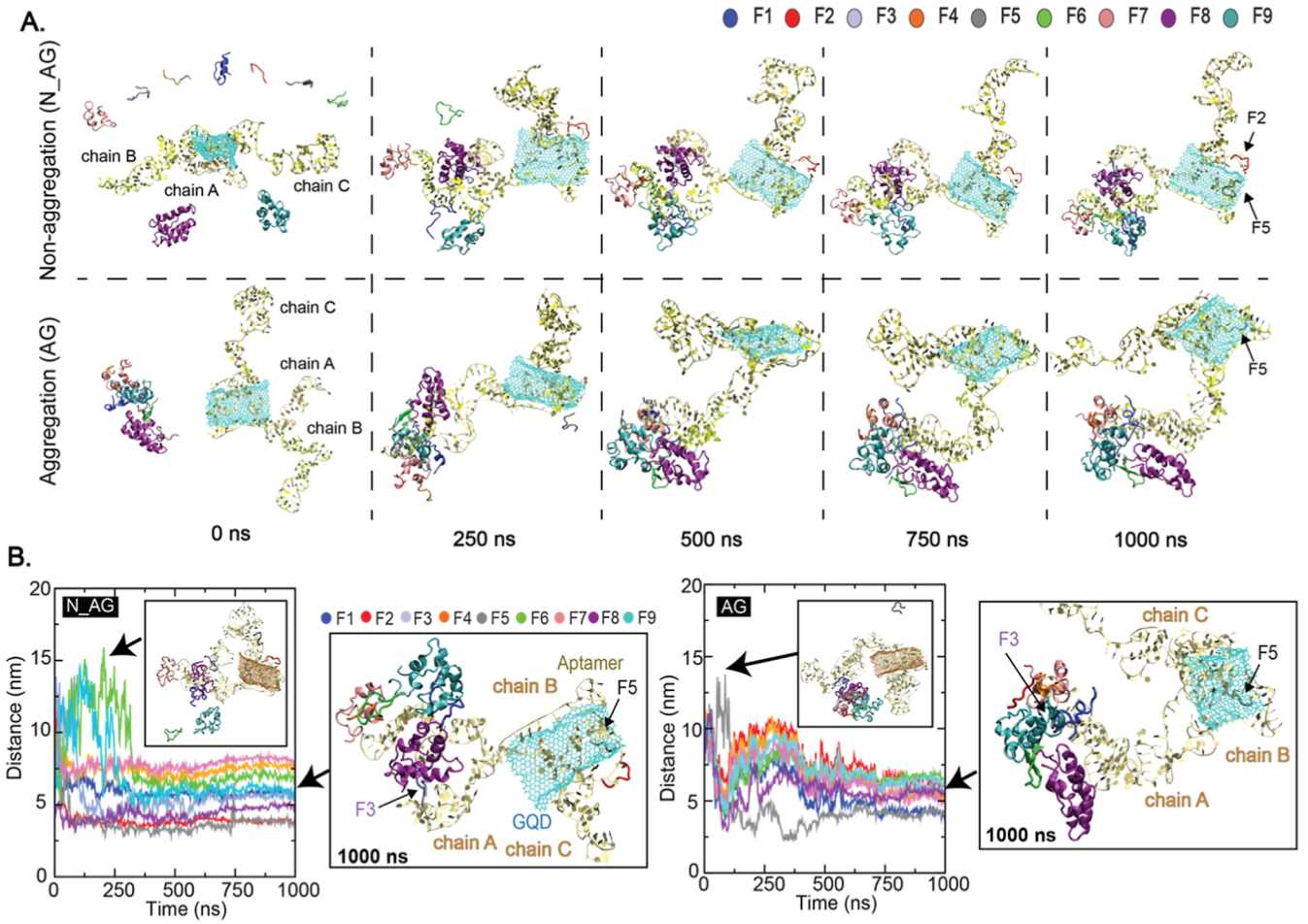

Figure 2. (A) Orientations of the fragment−GQDA complex as a function of time (at 0, 250, 500, 750, and 1000 ns). Three aptamers are shown in yellow. (B) Distances between centers of masses (COMs) of each fragment and GQDA in nonaggregation and aggregation systems as a function of time. The insets show the orientations of each fragment when they are away from a GQDA complex (left) and at 1000 ns (right).

counterions, and 1 M NaCl. Each residue was assigned a protonated state at a physiological pH.

Simulation Protocols. All simulations were performed using the GROMACS 2020.4 package (www.gromacs.org)[46] with the AMBER99SB-ILDN force field.[47] The energy minimization was run for 1000 steps using the steepest descent algorithm to remove bad contacts. The 10 ns equilibration run was carried out under an *NPT* ensemble using a v-rescaling thermostat.[48] The Particle Mesh Ewald (PME) sum was applied for the electrostatic treatment with a Fourier spacing of 0.12 nm, fourth-order spline interpolation, and a short-range cutoff of 1 nm.[49] Fragments, the GQDA complex, solvent, and ions were coupled independently at 300 K using a coupling constant τ_t = 0.1 ps. The Parrinello−Rahman algorithm was used for pressure control at 1 bar with a coupling constant of $\tau_{p=}$ 1 ps. A 2 fs time step was used. Then, the 1000 ns production run was further performed.

The data were analyzed using GROMACS commands. Visual molecular dynamics (VMD) was used for graphical images.[50,51] An initial structure from each production run was used as a reference for the *C*-alpha root-mean-square deviation (RMSD) and root-mean-square fluctuation (RMSF). The ″gmx do_dssp″ command was used to calculate the secondary structure. The hydrogen bonds were computed using ″gmx hbond″ with the default configuration (a cutoff radius of 0.35 nm and an angle of 30° between the hydrogen donor and acceptor).

RESULTS AND DISCUSSION

It is found in this work that the adsorption of albumin fragments on GQDA is spontaneous in all cases (Figure 2A). This is confirmed by the reduction in fragment−GQDA distances before reaching constant distances after 450 ns in all cases (Figure 2B). Although some fragments are scattered at the beginning, all cluster with GQDA within 450 ns (see the insets in Figure 2B). This indicates that the fragments prefer binding to GQDA rather than remaining in the bulk. A cluster of albumin fragments in AG appears to move slightly closer to a GQDA complex (distance range of 4−6.5 nm) compared to the N_AG condition (distance range of 4−7.5 nm; Figure 2B). The short distances of small fragments (F2 and F3 in N_AG and F1 and F3 in AG) indicate the closest binding to the GQDA complex (Figure 2B). Interestingly, the large fragment, F8, binds closely to a GQDA complex, whereas F9, which has a size comparable to that of F8, appears to stay further away from GQDA in all cases (Figure 2B). Most fragments seem to access and bind to parts of the aptamer that float in the bulk (Figure 2A).

As shown in Figure 3A, freely moving fragments in N_AG form more GQDA contacts than preclustered fragments in AG. Fragments in both N_AG and AG prefer binding to aptamers rather than GQDs. The assembly of fragments and GQDA appears to be driven by the aptamer−fragment interactions, even though clustered fragments in AG exhibit lower aptamer contact numbers (Figure 3A). Among all fragments, F1 and F8 in N_AG provide the highest contact numbers, indicating close packing to that of GQDA (Figure 3A).

https://doi.org/10.1021/acs.langmuir.5c00732
Langmuir 2025, 41, 11081−11089

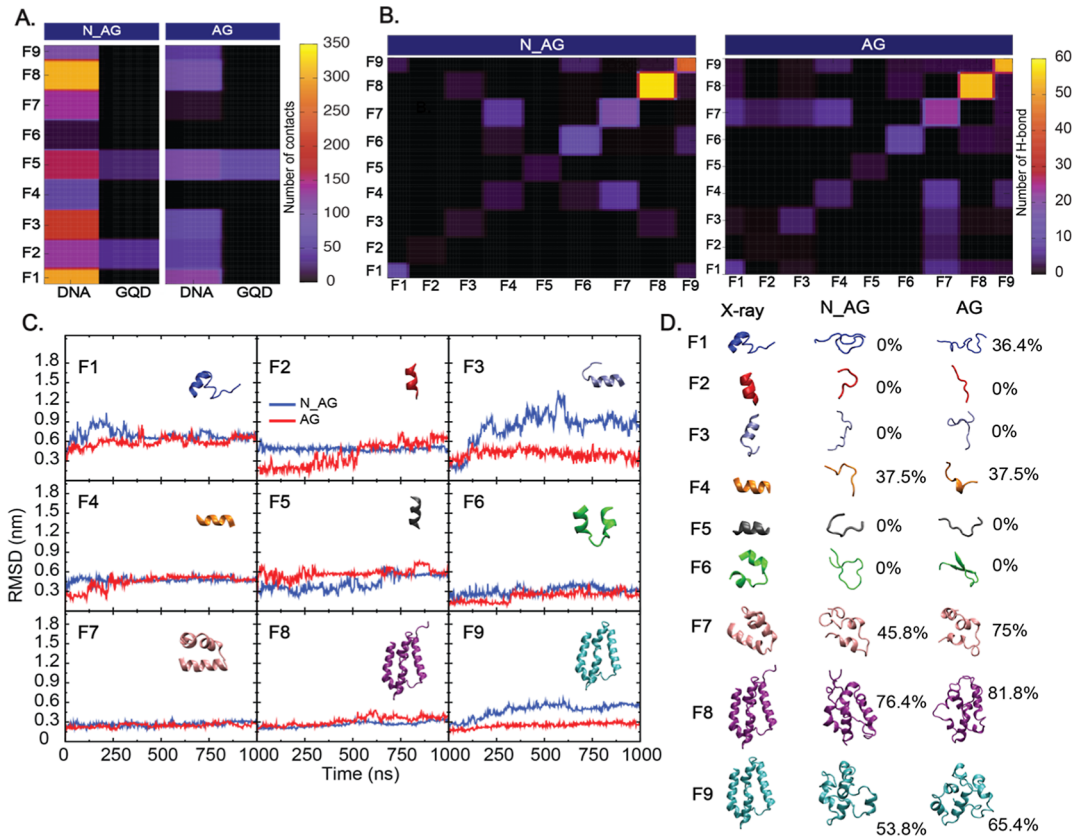

Figure 3. Contour maps of fragment−DNA aptamer and fragment−GQD contact numbers are shown in (A), where the intra- and inter-hydrogen bonds between fragments are displayed in (B). (C) C-alpha RMSFs of all fragments in both N_AG and AG systems. (D) Cartoon views of albumin fragments in N_AG and AG systems in a comparison to fragments obtained from a crystal structure (PDB code: 1E78). The percentages of helicities are also displayed on the right-hand side of each cartoon view.

Since GQD is saturated with aptamers, all fragments experience difficulty making direct contact with GQD. F2 and F5 in N_AG can bind to both aptamers and GQD, whereas in AG, only F5 interacts with both aptamers and GQD (Figures 2A and 3A). Additionally, fragments can also interact with other fragments, even in N_AG (Figure 3B). This self-aggregation can disrupt the adsorption of fragments on GQDA, leading to misleading results.

The C-alpha RMSDs are computed, as seen in Figure 3C, to observe protein flexibility. Overall, the fragments in AG appear to have a lower protein mobility than those of N_AG (Figure 3C). This is because all fragments in AG are preaggregated, leading to geometric confinement. The reduced protein flexibility observed in AG is therefore expected.

Considering each fragment, F1, F3, and F9 in N_AG show a higher structural flexibility (higher RMSDs) than those in AG (Figure 3C). The presence of GQDA in N_AG appears to enhance fragment flexibility compared to a previous work where the dynamics of each fragment in solution were investigated.[16] In particular, the short fragment F3 displays a high RMSD in N_AG because of its bound location on an aptamer surface, while F3 in AG is embedded in the fragment cluster (see insets in Figure 2A), resulting in a lower RMSD. This RMSD result is in good agreement with the RMSF results, as seen in Figure S2 in the Supporting Information.

To further determine protein properties, the percentages of helical contents of all fragments are computed, as seen in Figure 3D. The final snapshots of each fragment are also displayed for comparison with fragments obtained from a crystal structure (PDB code: 1E78). This helicity includes all types of helices (α-helix, 3-helix, and 5-helix).[52] Comparing N_AG and AG, the clustering of fragments can help preserve the protein structure. As expected, the short fragments (F1−F6) are unfolded, which is evident by the severe loss of % helicity in Figure 3D. F2, F3, F5, and F6 completely lose their secondary structure, whereas F1 and F4 maintain one-third of their helicity (~36−37% remaining helicity) (Figure 3D).

Considering the cartoon view and helicity content in Figure 3D, although F1 and F4 appear to lose the α-helix content, some regions of the fragments can turn into other types of helices, leading to the retention of helical contents (Table S1 in the Supporting Information). In the case of longer fragments (F7−F9), they preserve their secondary structures. Interestingly, F8, which was reported to be the most stable fragment in a previous work,[16] maintains most of its folds (~76−82% helicity). The high stability of F8 is in good agreement with a previous work.[16] The presence of GQDA does not disrupt the stability of the F8 core structure.

In contrast, F9, which is slightly shorter than F8 due to the absence of the latching loop, seems to lose approximately half of its structure during the GQDA−fragment assembly (see F8 and F9 structures in Figure S1C in the Supporting Information). The stability of the protein structure is also confirmed by the number of hydrogen bonds in Figure 3B. F8 is the most stable fragment due to its ability to form a large number of self-hydrogen bonds (Figure 3B).

Each fragment can also interact with other fragments, as well. N_AG seems to form fewer fragment−fragment

https://doi.org/10.1021/acs.langmuir.5c00732
Langmuir 2025, 41, 11081−11089

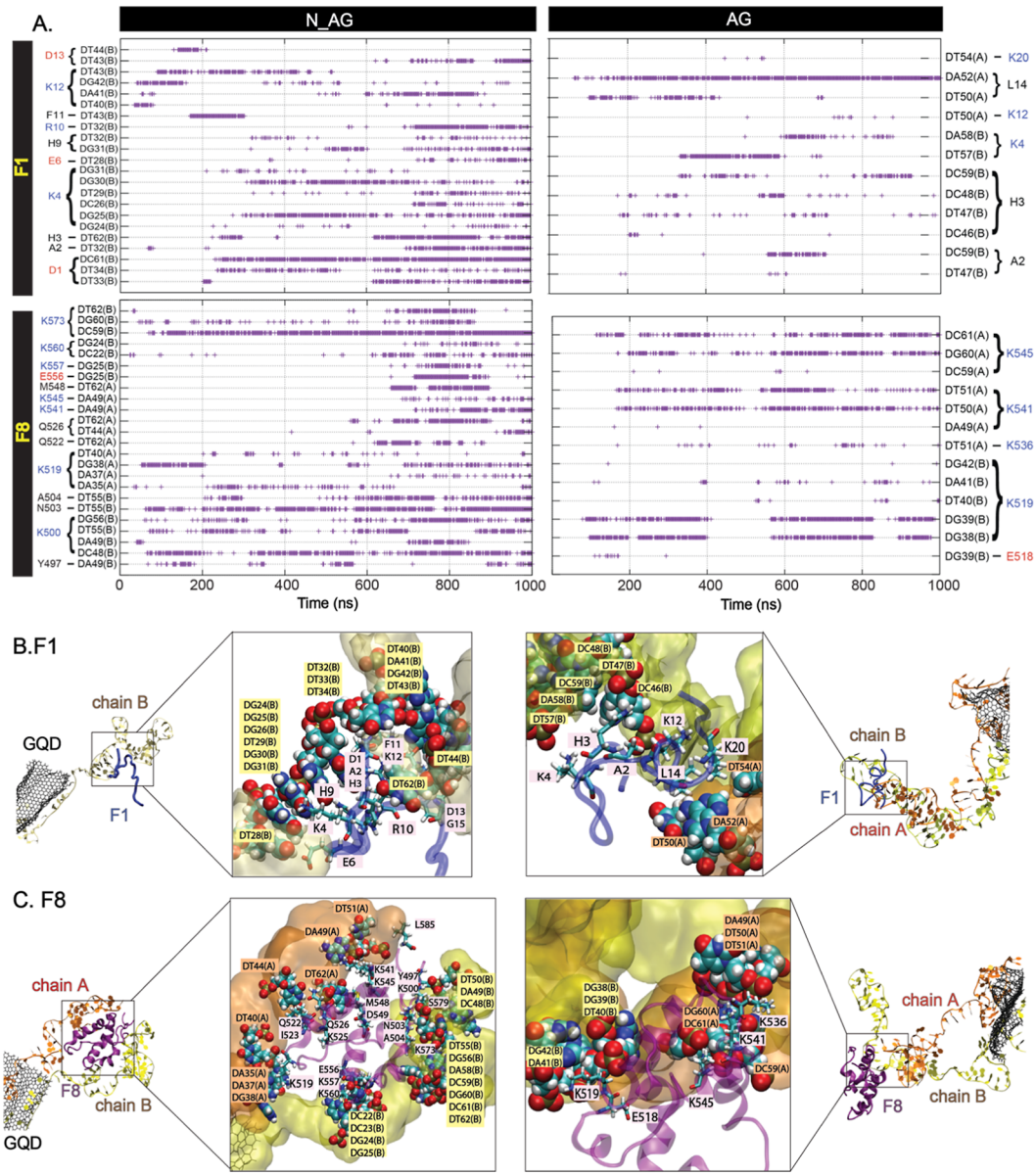

Figure 4. (A) Occurrence of hydrogen bonds between key residues of F1 and F8 and aptamers as a function of time, where their locations are shown in (B,C). Positively and negatively charged residues are colored blue and red, respectively. Aptamers are labeled in VDW format, whereas amino acids on fragments are displayed in licorice format.

interactions because such free fragments in N_AG bind closely to aptamers (Figure 3B). In contrast, the preaggregated fragments in AG show high fragment−fragment hydrogen bonds, which leads to fewer GQDA interactions (Figure 3A,B). In AG, the presence of hydrogen bonds between F7 and other fragments (F1−F4) suggests that F7 acts as the main anchor for other fragment deposition. Not only does this result in the alteration of secondary structure, but changes in electrostatic properties are also observed (Figure S3 in the Supporting Information). Only F8 appears to preserve its overall electrostatic properties (Figure S3).

To explore how fragments interact with aptamers, an in-depth hydrogen bond analysis is performed. Only the interactions of aptamers with F1 and F8 are shown here due to their strong binding (Figure 3A); however, the aptamer interactions with other fragments can be seen in Figures S4 and S5 in the Supporting Information. Both F1 and F8 can form strong interactions with aptamers in both N_AG and AG cases, but those in N_AG seem to bind more tightly to aptamers due to the higher number of hydrogen bonds (Figures 3A and 4A).

The aptamer−fragment hydrogen bond network appears to be dominated by charged residues, especially positively charged residues, such as lysines, in both N_AG and AG. Nonetheless, fragments in AG seem to form fewer interactions with aptamers due to its clustered conformation (Figure 4A). Like other fragments, F1 and F8 bind tightly to the GQDA complex through charged residues with the assistance of noncharged amino acids (Figure 4A). Compared to AG, the greater fragment flexibility in N_AG allows easier accessibility of fragments to aptamers, resulting in a higher number of aptamer−fragment hydrogen bonds (Figures 4A and S4 and S5 in the Supporting Information).

For F8, it clearly exhibits more fragment−aptamer interactions than for F1 (Figure 4A). This may be due to its larger size. In N_AG, F1 mainly employs three acidic (D1, E6,

https://doi.org/10.1021/acs.langmuir.5c00732
Langmuir 2025, 41, 11081−11089

and D13), three basic (K4, R10, and K12), and three nonpolar (A2, H3, and H9) residues to interact with aptamers, while F8 interacts with aptamers through seven basic (K500, K519, K541, K545, K557, K560, and K573), one acidic (E556), and two noncharged (N503 and A504) residues. The binding locations of key residues can be seen in Figure 4B,C.

In AG, more F8−aptamer interactions are observed, primarily from K519, K536, K541, and K545. The smaller F1 can form hydrogen bonds with aptamers via A2, H3, K4, K12, L14, and K20, with different degrees of interaction occupancies (Figure 4A). Interestingly, each basic residue can form multiple hydrogen bonds with a nucleotide. The presence of more positively charged (basic) residues can facilitate tighter fragment−aptamer binding (Figure S6A in the Supporting Information).

For N_AG, all fragments can directly interact with aptamers, whereas some fragments in AG fail to bind aptamers (Figures S4 and S5 in the Supporting Information). F6 appears to be unfavorable for aptamers due to its lack of interactions with aptamers (Figures S4 and S5).

Overall, F1 and F8 show the highest number of protein−aptamer interactions. In particular, F8, which is the most stable and maintained its folds,[16] retains its structure, allowing it to act as an aptamer recognition site. Lysine-rich areas seem to be a favorable site for aptamer binding (Figure S6A in the Supporting Information). The preserved structure and strong aptamer−F8 interactions suggest that F8 could serve as a potential biomarker for kidney disease. Its stability in urine, detectability using aptamer-based biosensors, and role as a distinct fragment of albumin suggest that F8 may indicate albumin degradation or abnormal kidney function. Our findings highlight F8 as a promising candidate for a novel kidney disease biomarker in urine, potentially detected by an aptasensor in a previous study.[11] Given its structural stability and strong aptamer interactions, F8 could offer additional diagnostic value beyond the total albumin measurement. Nonetheless, further experimental studies are needed to validate this hypothesis.

Considering the GQDA complex, aptamers appear to employ their 5′ terminus to adhere to GQD and leave the 3′ terminus in the bulk (Figure S6B in the Supporting Information). Thus, most fragments are complexed with aptamers at their 3′ end and remain in the bulk. Only F5 can attach to both GQD and the 5′ end of the aptamer (Figures 2B (insets), 3A, and S5 in the Supporting Information). Unlike microsized graphene/DNA adsorption,[53−55] the use of GQD appears to prevent the laying-flat conformation of aptamers, which facilitates the accessibility of probes and analytes.

CONCLUSION

In summary, the binding of urinary albumin fragments to aptamer-bound graphene quantum dots is studied. The binding of preaggregated (AG) and nonaggregated (N_AG) fragments to GQDA is examined. Our findings demonstrate the spontaneous assembly of the GQDA−fragment complex. Most fragments interact with aptamers, highlighting the importance of aptamer saturation on the GQD surface. Nonaggregated fragments have easier access to aptamers than aggregated fragments. This is because aggregated fragments are tightly packed, which induces geometric confinement and, sequentially, structural rigidity.

Nonetheless, some self-hydrogen bonds form between fragments in N_AG. This can hinder aptamer accessibility, which may sequentially lead to misleading results. Regarding aptamer−fragment binding, positively charged residues serve as key contributors to aptamer−fragment interactions. Lysine-rich regions on fragments appear to act as aptamer recognition sites. Both N_AG and AG exhibit similar binding patterns, where both F1 and F8 show a higher number of aptamer contacts than the other fragments under N_AG and AG conditions.

Notably, F8, which is the most stable and structurally preserved fragment, forms a high number of hydrogen bonds with aptamers, suggesting its potential as a urinary biomarker. In this work, fragment−aptamer desorption from the GQD was not observed throughout the course of simulation. This desorption phenomenon has been reported experimentally to occur on a minute time scale,[23,24] which cannot be captured by conventional MD simulations. Future studies employing accelerated simulation techniques may provide further insights into this process. Additionally, the effect of pH and ionic strength might alter the binding interaction,[56−58] requiring further investigation. The insights from this study will be instrumental in designing highly sensitive and selective detection strategies for urinary albumin fragments. Understanding the molecular interactions between albumin fragments and GQDA can help refine diagnostic approaches, ultimately enhancing CKD screening and monitoring. These findings pave the way for the development of more reliable and effective diagnostic platforms.

ASSOCIATED CONTENT

Supporting Information

The Supporting Information is available free of charge at https://pubs.acs.org/doi/10.1021/acs.langmuir.5c00732.

Details of aptamer-bound GQD as a function of time; latching loop of F8, which makes it different from F9; root-mean-square fluctuations (RMSFs) of fragments in N_AG and AG systems; electrostatic potentials calculated from APBS; hydrogen bonds between fragments and aptamer as a function of time; labeled position of aptamer binding to F1 and F8; and number of helical contents (PDF)

AUTHOR INFORMATION

Corresponding Authors

Deanpen Japrung − *National Science and Technology Development Agency, National Nanotechnology Center, Pathum Thani 12120, Thailand;* orcid.org/0000-0003-4206-6641; Phone: +66-2564-6555; Email: deanpen@nanotec.or.th

Prapasiri Pongprayoon − *Faculty of Science, Department of Chemistry, Kasetsart University, Bangkok 10900, Thailand; Center for Advanced Studies in Nanotechnology for Chemical, Food and Agricultural Industries, KU Institute for Advanced Studies, Kasetsart University, Bangkok 10900, Thailand;* orcid.org/0000-0002-1472-8241; Phone: +66-2562-5555; Email: fsciprpo@ku.ac.th

Author

Chanya Archapraditkul − *Faculty of Science, Department of Chemistry, Kasetsart University, Bangkok 10900, Thailand*

Complete contact information is available at:

https://pubs.acs.org/10.1021/acs.langmuir.5c00732

Notes

The authors declare no competing financial interest.

■ ACKNOWLEDGMENTS

We would like to thank the Kasetsart University Research and Development Institute (KURDI) (grant number: FF(KU) 51.67), the Health Systems Research Institute (grant number: 201215), the Fundamental Fund (grant number: 206998), and the High-Quality Research Graduate Development Cooperation Project between Kasetsart University and the National Science and Technology Development Agency (NSTDA) for financial support. We also thank Kasetsart University Computer Services (Nontri-AI) for computer facilities.

■ ABBREVIATIONS

HSA, human serum albumin
CKD, chronic kidney disease
MD, molecular dynamics
GQD, graphene quantum dot
GQDA, graphene−aptamer complex

■ REFERENCES

(1) Verma, A.; Schmidt, I. M.; Claudel, S.; Palsson, R.; Waikar, S. S.; Srivastava, A. Association of Albuminuria with Chronic Kidney Disease Progression in persons with chronic kidney disease and Normoalbuminuria: a cohort study. *Ann. Int. Med.* **2024**, *177* (4), 467−475.

(2) Heerspink, H. J. L.; Gansevoort, R. T. Albuminuria is an appropriate therapeutic target in patients with CKD: the pro view. *Clin. J. Am. Soc. Nephrol.* **2015**, *10* (6), 1079−1088.

(3) Hoerger, T. J.; Wittenborn, J. S.; Segel, J. E.; Burrows, N. R.; Imai, K.; Eggers, P.; Pavkov, M. E.; Jordan, R.; Hailpern, S. M.; Schoolwerth, A. C.; Williams, D. E. A health policy model of CKD: 2. The cost-effectiveness of microalbuminuria screening. *Am. J. Kidney Dis* **2010**, *55* (3), 463−473.

(4) Mathan Kumar, S.; Essakky, S.; Rajasulochana, S. R.; Kar, S. S.; Sivanatham, P.; Anandraj, J.; Parameswaran, S.; Soman, B.; Rajsekhar, K.; Stanley, A. Cost-effectiveness of population-based screening for microalbuminuria in people with type 2 diabetes mellitus in India. *Int. J. Technol. Assess Health Care* **2023**, *39* (1), No. e66.

(5) Busby, D. E.; Bakris, G. L. Comparison of commonly used assays for the detection of microalbuminuria. *J. Clin. Hypertens (Greenwich)* **2004**, *6* (s11), 8−12.

(6) Carroll, M. F.; Temte, J. L. Proteinuria in adults: a diagnostic approach. *Am. Fam. Physician* **2000**, *62* (6), 1333−1340.

(7) Mejia, J. R.; Fernandez-Chinguel, J. E.; Dolores-Maldonado, G.; Becerra-Chauca, N.; Goicochea-Lugo, S.; Herrera-Añazco, P.; Zafra-Tanaka, J. H.; Taype-Rondan, A. Diagnostic accuracy of urine dipstick testing for albumin-to-creatinine ratio and albuminuria: A systematic review and meta-analysis. *Heliyon* **2021**, *7* (11), No. e08253.

(8) Toto, R. D. Microalbuminuria: definition, detection, and clinical significance. *J. Clin. Hypertens (Greenwich)* **2004**, *6* (s11), 2−7.

(9) Yang, C. J.; Chen, D. P.; Wen, Y. H.; Lai, N. C.; Ning, H. C. Evaluation the diagnostic accuracy of albuminuria detection in semi-quantitative urinalysis. *Clin. Chim. Acta* **2020**, *510*, 177−180.

(10) Osberg, I.; Chase, H. P.; Garg, S. K.; DeAndrea, A.; Harris, S.; Hamilton, R.; Marshall, G. Effects of storage time and temperature on measurement of small concentrations of albumin in urine. *Clin. Chem.* **1990**, *36* (8), 1428−1430.

(11) Sompark, C.; Chawjiraphan, W.; Sukmak, M.; Cha'on, U.; Anutrakulchai, S.; Pongprayoon, P.; Putnin, T.; Pimalai, D.; Pinrod, V.; Japrung, D. Effects of Boric Acid and Storage Temperature on the Analysis of Microalbumin Using Aptasensor-Based Fluorescent Detection. *Biosensors (Basel)* **2022**, *12* (11), 915.

(12) Herrington, W.; Illingworth, N.; Staplin, N.; Kumar, A.; Storey, B.; Hrusecka, R.; Judge, P.; Mahmood, M.; Parish, S.; Landray, M.; Haynes, R.; Baigent, C.; Hill, M.; Clark, S. Effect of Processing Delay and Storage Conditions on Urine Albumin-to-Creatinine Ratio. *Clin J. Am. Soc. Nephrol.* **2016**, *11* (10), 1794−1801.

(13) Theodorescu, D.; Fliser, D.; Wittke, S.; Mischak, H.; Krebs, R.; Walden, M.; Ross, M.; Eltze, E.; Bettendorf, O.; Wulfing, C.; Semjonow, A. Pilot study of capillary electrophoresis coupled to mass spectrometry as a tool to define potential prostate cancer biomarkers in urine. *Electrophoresis* **2005**, *26* (14), 2797−2808.

(14) Kragh-Hansen, U. Possible Mechanisms by Which Enzymatic Degradation of Human Serum Albumin Can Lead to Bioactive Peptides and Biomarkers. *Front. Mol. Biosci.* **2018**, *5*, 63.

(15) Résimont, G.; Cavalier, E.; Radermecker, R.; Delanaye, P. Albuminuria in diabetic patients: how to measure it?-a narrative review. *J. Lab. Precis. Med.* **2022**, *7*, 4.

(16) Archapraditkul, C.; Janon, K.; Japrung, D.; Pongprayoon, P. Structural and dynamic properties of urinary human serum albumin fragments: a molecular dynamics study. *J. Biomol. Struct. Dyn.* **2024**, *42* (14), 7532−7540.

(17) Ghosh, S.; Datta, D.; Cheema, M.; Dutta, M.; Stroscio, M. A. Aptasensor based optical detection of glycated albumin for diabetes mellitus diagnosis. *Nanotechnology* **2017**, *28* (43), 435505.

(18) Ayodele, O. O.; Adesina, A. O.; Pourianejad, S.; Averitt, J.; Ignatova, T. Recent Advances in Nanomaterial-Based Aptasensors in Medical Diagnosis and Therapy. *Nanomaterials (Basel)* **2021**, *11* (4), 932.

(19) Putnin, T.; Waiwinya, W.; Pimalai, D.; Chawjiraphan, W.; Sathirapongsasuti, N.; Japrung, D. Dual sensitive and rapid detection of glycated human serum albumin using a versatile lead/graphene nanocomposite probe as a fluorescence−electrochemical aptasensor. *Analyst* **2021**, *146* (13), 4357−4364.

(20) Apiwat, C.; Luksirikul, P.; Kankla, P.; Pongprayoon, P.; Treerattrakoon, K.; Paiboonsukwong, K.; Fucharoen, S.; Dharakul, T.; Japrung, D. Graphene based aptasensor for glycated albumin in diabetes mellitus diagnosis and monitoring. *Biosens. Bioelec.* **2016**, *82*, 140−145.

(21) Sompark, C.; Chawjiraphan, W.; Sukmak, M.; Cha'on, U.; Anutrakulchai, S.; Pongprayoon, P.; Putnin, T.; Pimalai, D.; Pinrod, V.; Japrung, D. Effects of Boric Acid and Storage Temperature on the Analysis of Microalbumin Using Aptasensor-Based Fluorescent Detection. *Biosensors* **2022**, *12* (11), 915.

(22) Hatada, M.; Pavlidis, S.; Sode, K. Development of a glycated albumin sensor employing dual aptamer-based extended gate field effect transistors. *Biosens. Bioelectron.* **2024**, *251*, 116118.

(23) Chawjiraphan, W.; Apiwat, C.; Segkhoonthod, K.; Treerattrakoon, K.; Pinpradup, P.; Sathirapongsasuti, N.; Pongprayoon, P.; Luksirikul, P.; Isarankura-Na-Ayudhya, P.; Japrung, D. Sensitive detection of albuminuria by graphene oxide-mediated fluorescence quenching aptasensor. *Spectrochim. Acta A Mol. Biomol. Spectrosc.* **2020**, *231*, 118128.

(24) Chawjiraphan, W.; Apiwat, C.; Segkhoonthod, K.; Treerattrakoon, K.; Pinpradup, P.; Sathirapongsasuti, N.; Pongprayoon, P.; Luksirikul, P.; Isarankura-Na-Ayudhya, P.; Japrung, D. Albuminuria detection using graphene oxide-mediated fluorescence quenching aptasensor. *MethodsX* **2020**, *7*, 101114.

(25) Gozali Balkanloo, P.; Mohammad Sharifi, K.; Poursattar Marjani, A. Graphene quantum dots: synthesis, characterization, and application in wastewater treatment: a review. *Mater. Adv.* **2023**, *4* (19), 4272−4293.

(26) Ozhukil Valappil, M.; Alwarappan, S.; Pillai, V. Spotlighting graphene quantum dots and beyond: Synthesis, properties and sensing applications. *Appl. Mater. Today* **2017**, *9*, 350−371.

(27) Tabish, T.; Zhang, S. Graphene Quantum Dots: Syntheses, Properties and Biological Applications. In *Reference Module in Materials Science and Materials Engineering*, 2016; pp 171−192..

(28) Chung, S.; Revia, R. A.; Zhang, M. Graphene Quantum Dots and Their Applications in Bioimaging, Biosensing, and Therapy. *Adv. Mater.* **2021**, *33* (22), No. e1904362.

(29) Bressi, V.; Ferlazzo, A.; Iannazzo, D.; Espro, C. Graphene Quantum Dots by Eco-Friendly Green Synthesis for Electrochemical Sensing: Recent Advances and Future Perspectives. *Nanomaterials (Basel)* **2021**, *11* (5), 1120.
(30) Henna, T. K.; Pramod, K. Graphene quantum dots redefine nanobiomedicine. *Mater. Sci. Eng., C* **2020**, *110*, 110651.
(31) Zhang, H.; Wang, Y.; Zhao, D.; Zeng, D.; Xia, J.; Aldalbahi, A.; Wang, C.; San, L.; Fan, C.; Zuo, X.; Mi, X. Universal Fluorescence Biosensor Platform Based on Graphene Quantum Dots and Pyrene-Functionalized Molecular Beacons for Detection of MicroRNAs. *ACS Appl. Mater. Interfaces* **2015**, *7* (30), 16152−16156.
(32) Mansuriya, B. D.; Altintas, Z. Applications of Graphene Quantum Dots in Biomedical Sensors. *Sensors* **2020**, *20*, 1072.
(33) Singh, R. D.; Shandilya, R.; Bhargava, A.; Kumar, R.; Tiwari, R.; Chaudhury, K.; Srivastava, R. K.; Goryacheva, I. Y.; Mishra, P. K. Quantum Dot Based Nano-Biosensors for Detection of Circulating Cell Free miRNAs in Lung Carcinogenesis: From Biology to Clinical Translation. *Front. Genet.* **2018**, *9*, 616.
(34) Sittiwanichai, S.; Japrung, D.; Pongprayoon, P. The binding of apo and glucose-bound human serum albumins to a free graphene sheet in aqueous environment: Simulation studies. *J. Mol. Graph Model* **2022**, *110*, 108073.
(35) Aye, N. N. S.; Maraming, P.; Tavichakorntrakool, R.; Chaibunruang, A.; Boonsiri, P.; Daduang, S.; Teawtrakul, N.; Prasongdee, P.; Amornkitbamrung, V.; Daduang, J. A Simple Graphene Functionalized Electrochemical Aptasensor for the Sensitive and Selective Detection of Glycated Albumin. *Appl. Sci.* **2021**, *11* (21), 10315.
(36) Natmai, S.; Kuntip, N.; Japrung, D.; Pongprayoon, P. The aggregation of multiple miR-29a cancer biomarkers induced by graphene quantum dots: Molecular dynamics simulations. *J. Mol. Graph Model* **2022**, *116*, 108267.
(37) Traiphothon, D.; Awang, T.; Kuntip, N.; Japrung, D.; Pongprayoon, P. How a mixture of microRNA-29a (miR-29a) and microRNA-144 (miR-144) cancer biomarkers interacts with a graphene quantum dot. *J. Mol. Graph. Model.* **2025**, *134*, 108881.
(38) Sittiwanichai, S.; Archapraditkul, C.; Japrung, D.; Shigeta, Y.; Mori, T.; Pongprayoon, P. Aggregation of Apo/Glycated Human Serum Albumins and Aptamer-Saturated Graphene Quantum Dot: A Simulation Study. *Biochemistry* **2024**, *63* (13), 1697−1707.
(39) Williams-Noonan, B. J.; Kamboukos, A.; Todorova, N.; Yarovsky, I. Self-assembling peptide biomaterials: Insights from spontaneous and enhanced sampling molecular dynamics simulations. *Chem. Phys. Rev.* **2023**, *4* (2), 021304.
(40) Meli, M.; Morra, G.; Colombo, G. Investigating the mechanism of peptide aggregation: insights from mixed monte carlo-molecular dynamics simulations. *Biophys. J.* **2008**, *94* (11), 4414−4426.
(41) Hjalte, J.; Hossain, S.; Hugerth, A.; Sjögren, H.; Wahlgren, M.; Larsson, P.; Lundberg, D. Aggregation Behavior of Structurally Similar Therapeutic Peptides Investigated by (1)H NMR and All-Atom Molecular Dynamics Simulations. *Mol. Pharmaceutics* **2022**, *19* (3), 904−917.
(42) Iscen, A.; Kaygisiz, K.; Synatschke, C. V.; Weil, T.; Kremer, K. Multiscale Simulations of Self-Assembling Peptides: Surface and Core Hydrophobicity Determine Fibril Stability and Amyloid Aggregation. *Biomacromolecules* **2024**, *25* (5), 3063−3075.
(43) Rissanou, A. N.; Keliri, A.; Arnittali, M.; Harmandaris, V. Self-assembly of diphenylalanine peptides on graphene via detailed atomistic simulations. *Phys. Chem. Chem. Phys.* **2020**, *22* (47), 27645−27657.
(44) Hughes, Z. E.; Walsh, T. R. What makes a good graphene-binding peptide? Adsorption of amino acids and peptides at aqueous graphene interfaces. *J. Mater. Chem. B* **2015**, *3* (16), 3211−3221.
(45) Panman, W.; Japrung, D.; Pongprayoon, P. Exploring the interactions of a DNA aptamer with human serum albumins: simulation studies. *J. Biomol. Struct. Dyn.* **2017**, *35* (11), 2328−2336.
(46) Van Der Spoel, D.; Lindahl, E.; Hess, B.; Groenhof, G.; Mark, A. E.; Berendsen, H. J. GROMACS: fast, flexible, and free. *J. Comput. Chem.* **2005**, *26* (16), 1701−1718.
(47) Lindorff-Larsen, K.; Piana, S.; Palmo, K.; Maragakis, P.; Klepeis, J. L.; Dror, R. O.; Shaw, D. E. Improved side-chain torsion potentials for the Amber ff99SB protein force field. *Proteins* **2010**, *78* (8), 1950−1958.
(48) Bussi, G.; Donadio, D.; Parrinello, M. Canonical sampling through velocity rescaling. *J. Chem. Phys.* **2007**, *126* (1), 014101.
(49) Darden, T.; York, D.; Pedersen, L. Particle mesh Ewald: An N·log(N) method for Ewald sums in large systems. *J. Chem. Phys.* **1993**, *98* (12), 10089−10092.
(50) Humphrey, W.; Dalke, A.; Schulten, K. V. M. D. VMD: Visual molecular dynamics. *J. Mol. Graph.* **1996**, *14* (1), 33−38.
(51) Spivak, M.; Stone, J.; Ribeiro, J.; Saam, J.; Freddolino, P.; Bernardi, R.; Tajkhorshid, E. VMD as a Platform for Interactive Small Molecule Preparation and Visualization in Quantum and Classical Simulations. *J. Chem. Inf. Model.* **2023**, *63*, 4664−4678.
(52) Nagy, G.; Oostenbrink, C. Dihedral-based segment identification and classification of biopolymers I: proteins. *J. Chem. Inf. Model.* **2014**, *54* (1), 266−277.
(53) Sun, J.; Li, Y.; Lin, J. Studying the adsorption of DNA nanostructures on graphene in the aqueous phase using molecular dynamic simulations. *J. Mol. Graph. Model.* **2017**, *74*, 16−23.
(54) Muraru, S.; Samoila, C. G.; Slusanschi, E. I.; Burns, J. S.; Ionita, M. Molecular dynamics simulations of DNA adsorption on graphene oxide and reduced graphene oxide-PEG-NH2 in the presence of Mg2+ and Cl− ions. *Coatings* **2020**, *10* (3), 289.
(55) Chen, J.; Chen, L.; Wang, Y.; Chen, S. Molecular dynamics simulations of the adsorption of DNA segments onto graphene oxide. *J. Phys. D: Appl. Phys.* **2014**, *47* (50), 505401.
(56) Scott, S.; Shaheen, C.; McGuinness, B.; Metera, K.; Kouzine, F.; Levens, D.; Benham, C. J.; Leslie, S. Single-molecule visualization of the effects of ionic strength and crowding on structure-mediated interactions in supercoiled DNA molecules. *Nucleic Acids Res.* **2019**, *47* (12), 6360−6368.
(57) Overman, L. B.; Lohman, T. M. Linkage of pH, Anion and Cation Effects in Protein-Nucleic Acid Equilibria: Escherichia coli SSB Protein-Single Stranded Nucleic Acid Interactions. *J. Mol. Biol.* **1994**, *236* (1), 165−178.
(58) da Rocha, L.; Baptista, A. M.; Campos, S. R. R. Computational Study of the pH-Dependent Ionic Environment around β-Lactoglobulin. *J. Phys. Chem. B* **2022**, *126* (45), 9123−9136.

https://doi.org/10.1021/acs.langmuir.5c00732
Langmuir 2025, 41, 11081−11089